Contents lists available at ScienceDirect

# Solid State Sciences

# Lanthanum strontium cobaltite as interconnect in oxide thermoelectric generators

Reshma K. Madathil, Truls Norby *

*Department of Chemistry, Centre for Materials Science and Nanotechnology, University of Oslo, FERMiO, Gaustadalléen 21, NO-0349, Oslo, Norway*

## ARTICLE INFO

## ABSTRACT

Issues related to use of metallic interconnects in oxide thermoelectric generators (TEGs) need to be addressed to secure performance and durability. Metal interconnects suffer from high cost of noble metals or chemical instability and contact resistance of non-noble metals, arising from oxidation, evaporation, and delamination in the oxidising conditions of ambient air at high operating temperatures. This work introduces the use of a stable and highly conducting ceramic oxide, in our case p-type lanthanum strontium cobaltite (La$_{0.6}$Sr$_{0.4}$CoO$_3$, LSC) as interconnect. We verified the thermochemical stability of LSC in contact with p-type Ni$_{0.98}$Li$_{0.02}$O (Li–NiO) and n-type Zn$_{0.98}$Al$_{0.02}$O (Al–ZnO) and examined the electrical characteristics. An area specific contact resistance (ASR$_c$) of ~1800 $\Omega$ cm$^2$ for a direct p-n junction was reduced to ~400 m$\Omega$ cm$^2$ for a p-LSC-n junction at a temperature of 300 °C, validating the concept. The use of a screen-printed LSC/Al–ZnO composite as a thin interconnect layer was found to decrease the contact resistance of the junction further to ~260 m$\Omega$ cm$^2$ at 300 °C, attributed to increased effective area of the LSC/Al–ZnO p-n junction.

## 1. Introduction

Oxide thermoelectric generators (TEGs) have potential advantages over non-oxides in terms of stability at higher temperatures under oxidising conditions (ambient air), non-toxicity, and low cost [1]. To meet industrial demands, the figure of merit ($zT$) of oxide thermoelectrics needs to improve, however, and focus has hence primarily been on the properties of the thermoelectric (TE) materials, while the stability and resistance of interconnects and interfaces have been less investigated [2]. The contact resistance $R_c$ at the interfaces reduces the $ZT$ of the device from that of the materials ($zT$)$_{thermoelement}$ according to [3,4].

$$(ZT)_{Device} = \frac{L}{(L + 2R_c\sigma)}(zT)_{thermoelement} \tag{1}$$

Here, $L$ is the device leg length, $R_c$ is the sum of contact resistances, $\sigma$ is the average bulk electrical conductivity and ($zT$)$_{thermoelement}$ is the average $zT$ of the thermoelement. Noble metals Ag, Au, and Pt and non-noble metals such as Ni, W, Cu, Fe, and Mo are commonly used as interconnect materials in conventional TEGs [5–8]. Generally, they are not suitable for oxide TEGs due to the high cost of the noble metals and oxidation of the non-noble metals, with formation of resistive layers and delamination as result [2,4,9–13]. In addition comes the problem of

blocking rectifying junctions between noble metals and oxides. According to the ideal Mott-Schottky theory, the work function ($\Phi$) of the metal and semiconductor determines the nature of the junction. For a p-type semiconductor, a metal with a higher work function than the p-type semiconductor forms a rectifying junction ($\Phi_m < \Phi_p$, rectifying) and leads to an ohmic contact if $\Phi_m > \Phi_p$. Similarly, for an n-type conductor, $\Phi_m > \Phi_n$ gives rectifying contact and become ohmic if $\Phi_m < \Phi_n$. In this sense, conventional metal contacts like Pt, Au and Ag are not suitable candidates for both NiO- and ZnO-based thermoelectrics. For example, Pt ($\Phi_{Pt} \sim 5.5$ eV) forms an ohmic contact with NiO ($\Phi_{NiO} \sim 5.2$ eV) and a Schottky contact with ZnO ($\Phi_{ZnO} \sim 4.5$ eV).

Some conventional metal interconnects like Ag, Au, Pt, Ni, and W have still been used in oxide devices [9,14]. In 2004, Funahashi et al. reported an interconnect consisting of Ag paste and oxide powders that enhanced the device efficiency of a p-type Ca$_{2.7}$Bi$_{0.3}$Co$_4$O$_9$ and n-type La$_{0.9}$Bi$_{0.1}$NiO$_3$ system [15]. Afterwards, other oxide-based TEGs were made using the same concept of a composite of metal and oxide interconnects but still based on noble metals. Later on, Holgate et al. reported that a Fe–Cr alloy could be considered for cobaltite based thermoelectrics [16].

In the present work we study the use of a highly conducting oxide as thermodynamically stable noble metal free interconnect to decrease the

---

* Corresponding author.
  *E-mail address:* truls.norby@kjemi.uio.no (T. Norby).
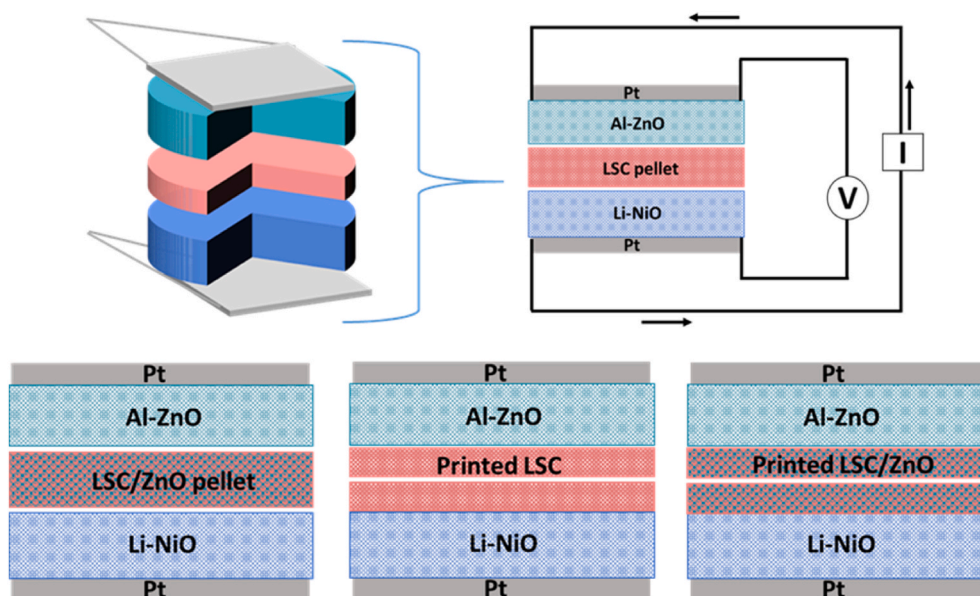
**Fig. 1.** Schematic diagram of assemblies used for electrical characterisation.

contact resistance between the legs of oxide TE elements. Our choice of interconnect material fell on perovskite-type lanthanum cobaltite $LaCoO_3$ (LC) acceptor-substituted 40% with Sr to form $La_{0.6}Sr_{0.4}CoO_3$ (LSC) with a conductivity of $4.4 \times 10^3$ S cm$^{-1}$ [17] at room temperature. We investigated the use of LSC between oxide TE materials p-type $Ni_{0.98}Li_{0.02}O$ (Li–NiO) and n-type $Zn_{0.98}Al_{0.02}O$ (Al–ZnO) in a p-LSC-n junction, hereafter p-L-n, as well as interfacial reactions and stability of the individual interfaces. LSC is a p-type oxide and hence the p-L-n assembly is effectively a p-p-n junction. Hence, the p-n junction between the LSC and Al–ZnO may expectedly be a major contributor to the overall resistance, and to reduce this, we made and characterised junctions with composite Al–ZnO + LSC interconnects, termed p-LZ-n.

## 2. Experimental

### 2.1. Materials synthesis

The Li–NiO and Al–ZnO used in this study were synthesised using a ball milling method as described previously [18,19]. LSC powder was synthesised by solid-state reaction based on details in published reports [17,20–22] with some modifications. The precursors $La_2O_3$, $Co_3O_4$ and $SrCO_3$ from Sigma-Aldrich of 99.9% purity were pre-annealed separately in ambient air at 600 °C before weighing. For $La_{0.6}Sr_{0.4}CoO_3$ the precursors were mixed in their stoichiometric ratio in 2-propanol in a planetary ball mill with zirconia jar and balls for 5 h. The resultant mixture was dried at 120 °C, followed by calcination at 800 °C for 5 h in air. The powder was grinded in an agate mortar for rehomogenisation followed by a second firing at 1050 °C in air. Part of the powder was pressed into pellets and sintered at 1300 °C for 10 h in air. The rest was used to fabricate a p-n composite of LSC and Al–ZnO. For this, the desired amounts of LSC and Al–ZnO were mixed in a rolling ball mill for 20 h in 2-propanol. After drying at 120 °C, a portion of the powder was pressed into a pellet and sintered at 1100 °C for 10 h in air.

### 2.2. Materials characterisation

The crystal structure and phase purity of LSC and LSC/Al–ZnO composite samples were analysed by powder X-ray diffraction (XRD) using a Bruker D8 diffractometer with CuKα radiation at room temperature. To understand the chemical interaction between the interconnect and thermoelements, we mixed LSC with Li–NiO and Al–ZnO in 50:50
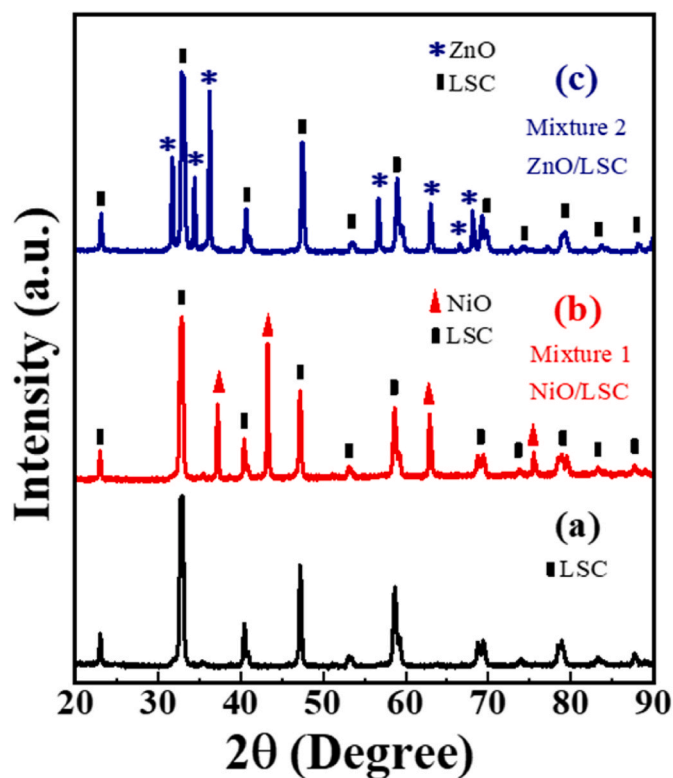


**Fig. 2.** X-ray diffraction patterns of (a) calcined $La_{0.6}Sr_{0.4}CoO_3$ powder (b) mixture of LSC with Li–NiO and (c) LSC with Al–ZnO after 100 h of heat treatment at 1100 °C.

vol% ratio and heated at 1100 °C for 100 h in air. The resultant powder was analysed using XRD. The microstructure and morphology of the sintered LSC pellets, composite pellets, and interfaces were investigated using an FEI Quanta 200 F FEG-ESEM Scanning Electron Microscope (SEM). The band gaps were calculated via UV–Vis spectroscopy using Tauc plots based on optical absorption properties measured at room temperature with a UV–Vis spectrophotometer (SPECORD® 200 PLUS, data analysis with spectroanalytical software WinASPECT PLUS).
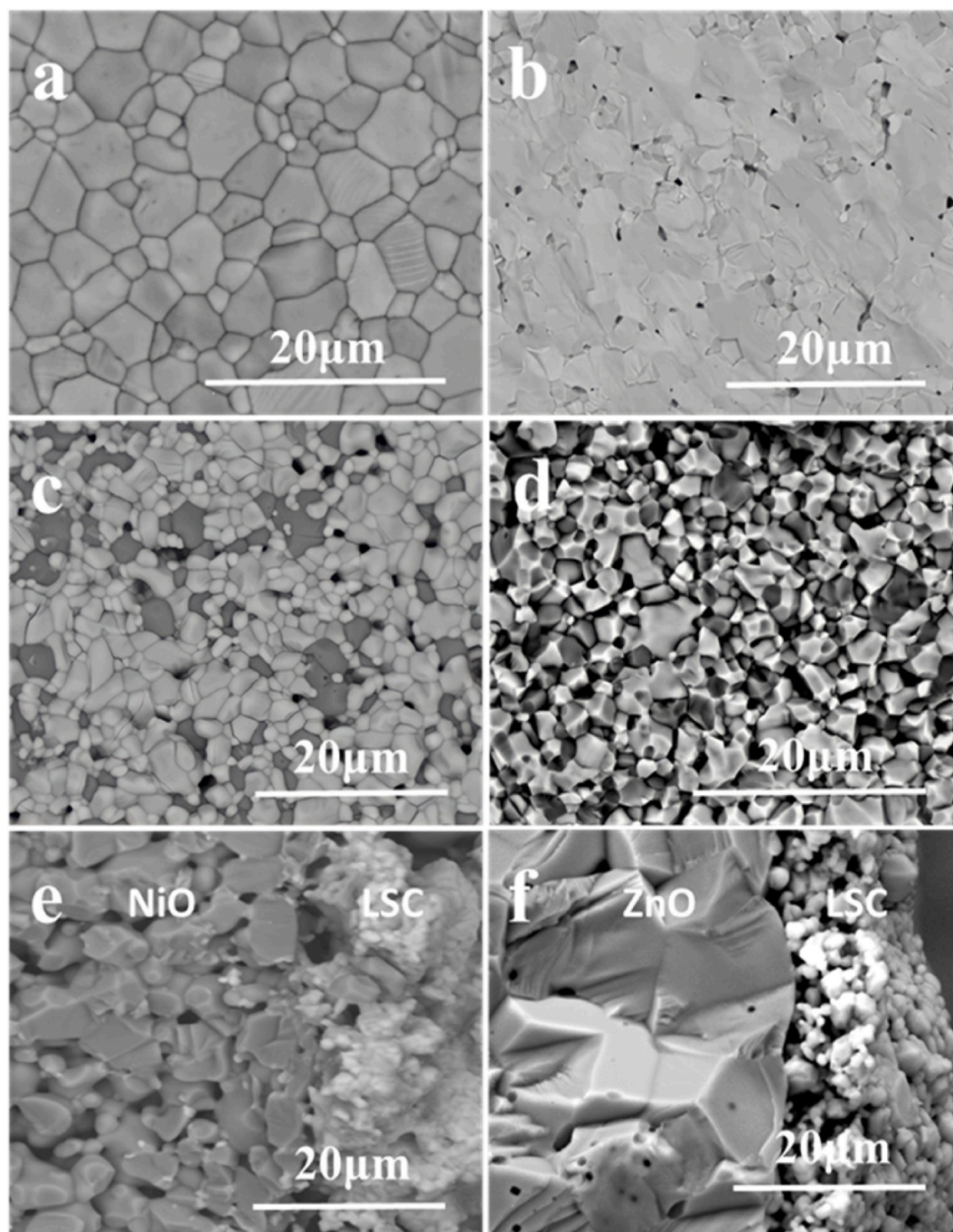
**Fig. 3.** SEM secondary electron detector images of a) surface and b) fracture cross-section of sintered LSC pellet. SEM back scattered electron images of c) surface and (d) fracture cross-section of LSC/Al–ZnO composite pellet. Bright grains represent LSC, dark grains represent Al–ZnO. SEM back scattered electron images of fracture cross sections of the interfaces between screen-printed LSC and (e) Li–NiO and (f) Al–ZnO.

### 2.3. Electrical measurements

A schematic illustration of the electrical measurement assembly used in this study is shown in Fig. 1. We used two different methods to make the interconnect contacts. The first method uses the interconnect in the pellet form with a contact area of ~2 cm², in which the LSC pellet is sandwiched between the two oxide TE pellets. The stacks of the 3 pellets were horizontally placed and spring-loaded in a ProboStat™ measurement cell (NORECS, Norway). The acronym p-L$_p$-n denotes this configuration, while when used with a composite pellet it is denoted p-LZ$_p$-n. In the other method, we used screen-printing to make 15–20 μm layers of the interconnect on both the p-and n-type pellets, termed as p-L$_S$-n for

printed LSC and p-LZ$_S$-n for printed LSC/Al–ZnO composite. The back side of each semiconductor was painted with Pt paste (METALOR®) and contacted by flat Pt mesh electrode connects each with two wires for current and voltage. All electrical measurements were done from 300 °C to 1000 °C in ambient air using a Gamry Reference 3000 potentiostat. The total resistance for the entire cell configuration was measured, and the area-specific resistance (*ASR*) of the junction and interconnect is reported here after deducting the resistance contributions of the metal oxide and metal contacts, based on separate measurements.
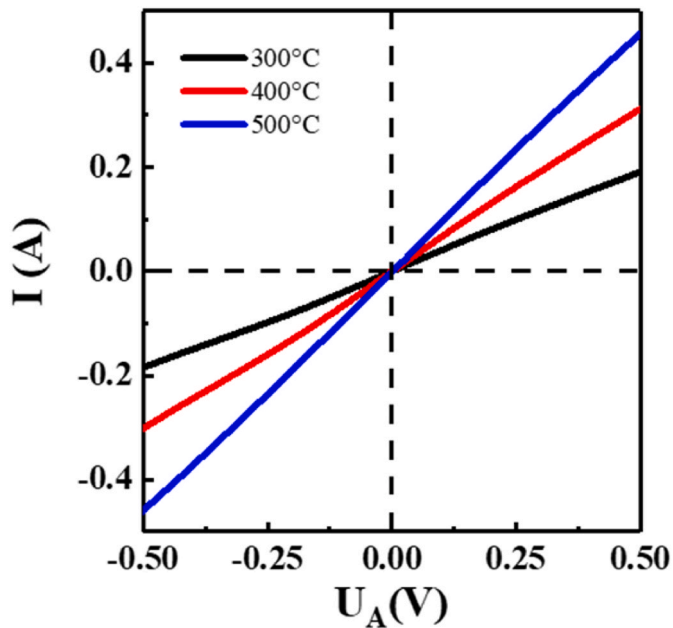
**Fig. 4.** I-$U_A$ curves of the p-$L_p$-n (Li–NiO/LSC/Al–ZnO) junction at three different temperatures.

## 3. Results and discussion

Fig. 2 (b) and (c) show the original phases of all mixed oxides without change in XRD peak positions after the heat treatments. Within the detection limits of this study, there is hence no chemical reaction between LSC and Li–NiO or Al–ZnO well above the temperature range used for measurements.

Fig. 3 a and b show, respectively, surface and cross-sectional morphologies of the LSC pellet with an average grain size ~3 μm and relative density higher than 90%, confirming also its phase purity. Fig. 3(c) and d are backscatter electron images of a surface and cross-section of an LSC/Al–ZnO (80:20 vol%) composite pellet.

Further SEM analyses of cross-sections of screen-printed LSC layers on Li–NiO and Al–ZnO pellet substrates are shown in Fig. 3(e) and f. They indicate that the LSC layer has good adherence to both semiconductor surfaces. No additional phases were detected in the SEM, confirming the absence of chemical reactions between the LSC interconnect and TE materials.

Interdiffusion of Co into NiO is still expected, forming solid solutions $Ni_{1-x}Co_xO$ and $La_{1-x}Sr_xCo_{1-y}Ni_yO_3$ [23], but the bulk and grain boundary diffusivities are limited [24] and since temperatures and times used were modest, we were unable to detect it by XRD or SEM. Moreover, it is known that substitution of Co for Ni enhances the p-type conductivity of NiO via the generation of holes and if there is a considerable amount of Co substitution it will further enhance the electrical conductivity of the system [25]. Ni-substitution in LSC has furthermore been reported to increase the electronic conductivity [26] and hence, interdiffusion of Co and Ni should improve electrical properties, but we did not notice considerable change, and conclude that interdiffusion was not significant.

We investigated the electrical properties of the Li–NiO/LSC/Al–ZnO (entire cell with all resistance contribution) assembly using current-voltage (I-$U_A$) measurements, and the results at three different temperatures are plotted in Fig. 4. The linear nature of the I-$U_A$ plot show that the LSC interface contacts are ohmic.

The temperature dependencies of area specific contact resistance for a direct p-n junction and junction with LSC pellet at the interface (p-$L_p$-n) are displayed in Fig. 5(a) while those for the pellet LSC (p-$L_p$-n) and a screen-printed LSC interface (p-$L_s$-n) are compared in Fig. 5(b). The resistance for the direct Li–NiO/Al–ZnO p-n junction was very high, attributed to the Schottky contact between NiO and ZnO [27,28]. The measured ASR was around 58 Ω cm² at 600 °C and 1800 Ω cm² at 300 °C which are similar to literature values for this type of junction [18]. The junction resistance decreases with increasing temperature and approaches a linear (ohmic) I-$U_A$ behaviour at 1000 °C.

The junction with an LSC pellet incorporated (p-$L_p$-n) showed in comparison an ASR of 400 mΩ cm² at 300 °C, four orders of magnitude lower than that of the direct junction at the same temperature.

The activation energy for the junctions incorporating LSC is slightly higher than the reported activation energy (~0.4 eV) of conduction in LSC [29], and may reflect interface resistance and remaining uncorrected TE materials resistances [30,31]. The slight decrease in resistance for p-$L_s$-n (Fig. 5(b)) compared with p-$L_p$-n can in part be attributed to the better adherence of the printed LSC interconnect to Li–NiO and Al–ZnO than possible in the pellet stack.

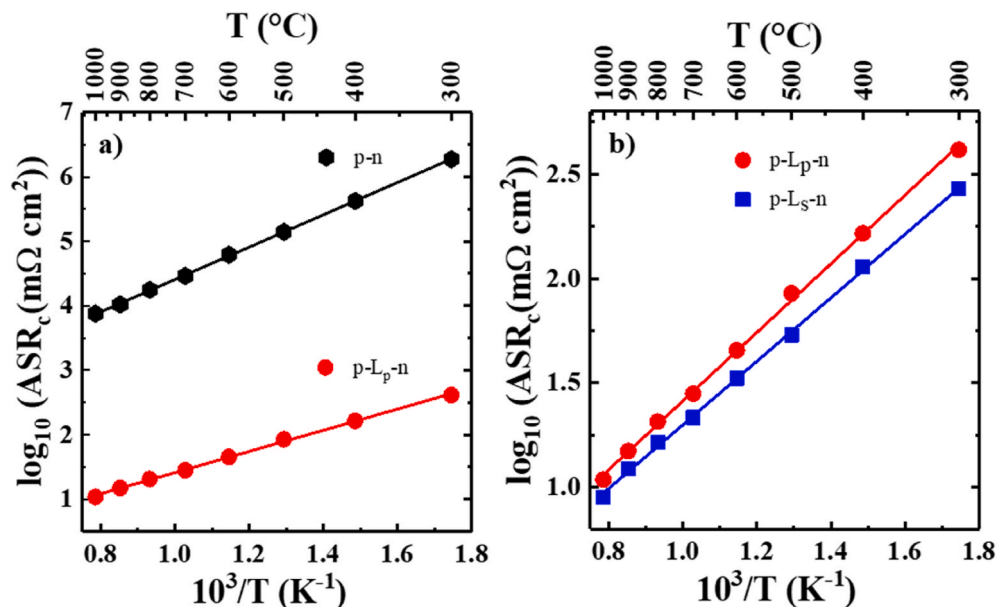Application of LSC as an interconnect between TE oxide materials



**Fig. 5.** Logarithmic values of area specific resistance as a function of inverse temperature for (a) p-n and p-$L_p$-n and for (b) p-$L_p$-n and p-$L_s$-n.
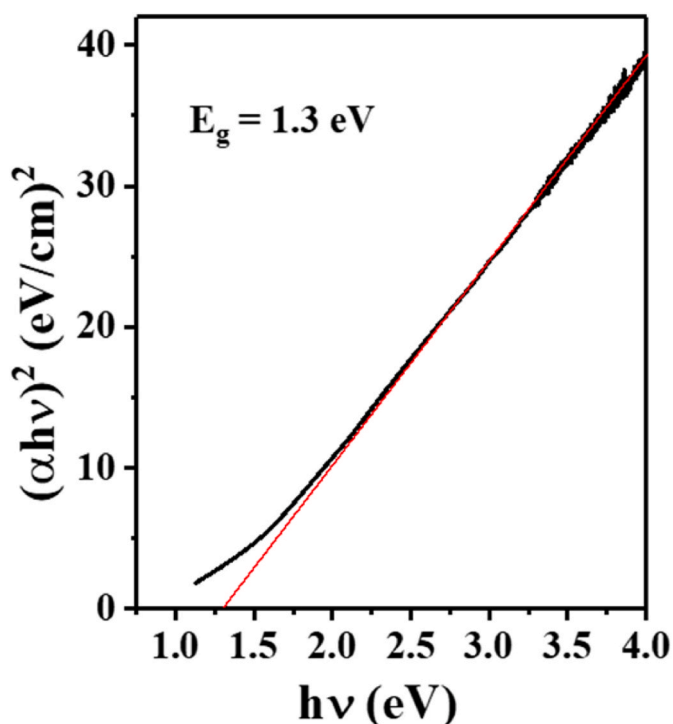
**Fig. 6.** Tauc plot based on UV–Vis absorption spectrum for estimation of band gap of LSC.

appears to decrease the overall system resistance due to formation of non-rectifying low-resistive interfaces. It is of interest to seek to understand this in terms of the band alignment between the interconnect and the TE materials. The band energy for the as prepared LSC was estimated using a Tauc plot (see Fig. 6). The bandgap of the LSC sample at room temperature was compared to its parental compound $LaCoO_3$ (LC, band gap at room temperature) to show the trend with Sr doping. LSC shows a strong and broad absorption peak in the visible region, and a band gap energy of 1.3 eV was then measured from tangent lines in the Tauc plot, which is somewhat lower than DFT-calculated and experimentally measured band gap energies reported for undoped LC [32–34].

In the p-L-n system, LSC forms an isotype p-p junction with NiO, while, a p-n heterojunction is formed between LSC and ZnO; hence, the overall p-L-n system contains a double heterostructure. To illustrate the main features of the junction, we developed the band diagram in Fig. 7 based mainly on computational and experimental results from literature combined with our abovementioned experimental results.

As a preliminary interpretation, the lower electrical resistance at the p-L-n (p−p−n) interface can be a consequence of the intermediate band

levels of LSC and hence reduction in the depth and length of depletion towards both NiO and ZnO as compared to a direct NiO–ZnO interface.

A composite interconnect made with LSC and Al–ZnO was used for further reduction of the resistance at the LSC/Al–ZnO junction. Fig. 8(a) shows the resistance of various p-LZ-n interfaces made with five composite compositions, $LZ_1$–$LZ_5$, corresponding to 20:80, 35:65, 50:50, 65:35 and 80:20 vol% of LSC:Al–ZnO, see Table 1. $LZ_5$ with the highest LSC content performs best, and the only one performing better than pure LSC. It was then used as a screen-printed electrode (p-$LZ_{5s}$-n) to improve the interface further and compared with the p-$L_s$-n. The results in Fig. 8 (b) shows that the composite p-$LZ_{5s}$-n configuration has the lowest resistance. The activation energy values calculated from the Arrhenius plot did not show much change for different LSC:ZnO compositions which implies that the interface barrier height is not influenced and that, therefore, the LSC-ZnO interfaces are essentially the same in the case of the pure LSC and the composite. However, the preexponential factor for resistance ($A_R$) decreased from ~5 mΩ cm$^2$ for $LZ_1$ to ~0.4 mΩ cm$^2$ for $LZ_5$. This may be attributed to the intended larger interface area in the composite. The presence of a more continuous path of highly conducting LSC phase in $LZ_5$ appears more beneficial than highly percolating Al–ZnO in the other composites.

## 4. Conclusions

In summary, we have investigated the use of highly conducting LSC as an oxide interconnect between the p-type Li-doped NiO and n-type Al-doped ZnO legs of a TE couple at 300–1000 °C in air. XRD and SEM show that LSC is stable at 1000 °C towards both Li–NiO and Al–ZnO, forming well-adherent contacts by firing of screen printed layers. The area-specific resistance of the p-n junction was drastically decreased by applying a pellet of LSC as interconnect, e.g. from ~1800 Ω cm$^2$ for the direct p-n junction to ~400 mΩ cm$^2$ for the p-L-n assembly at 300 °C, attributed to a lowering of the activation energy, reflecting the different band alignments. At the same temperature, the use of an LSC/Al–ZnO composite as interconnect reduced the ASR$_c$ further to ~260 mΩ cm$^2$, attributed to an enlarged active interface area between p-type LSC and n-type Al–ZnO. The optimal composite had a high LSC content (80:20 vol% LSC:Al–ZnO). This study demonstrates that air-stable, highly conducting oxides can be used as interconnects for high temperature oxide thermoelectrics, alleviating the need for expensive noble metals. Contact resistances can be further reduced by composites with one of the leg materials, and bonding can be done by screen-printing and firing of pastes of the interconnect.

## Author statement

RKM: Investigation, Methodology, Validation, Writing – original draft. TN: Conceptualization, Funding acquisition, Project administration, Resources, Supervision, Writing – review & editing.
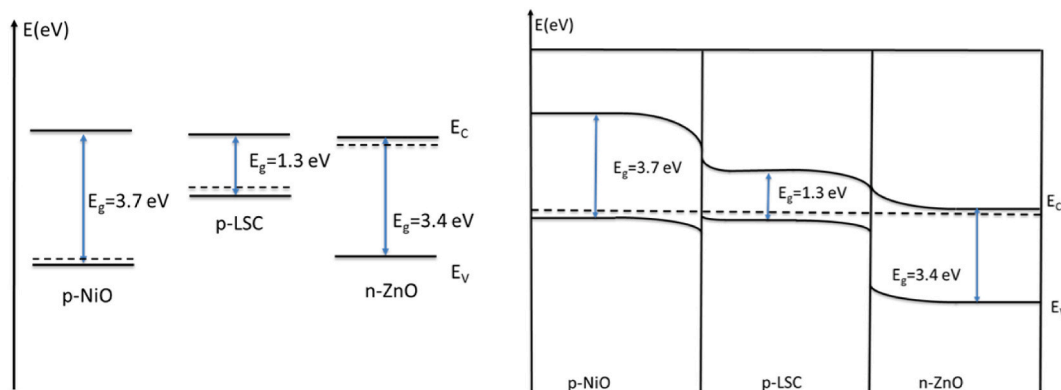
**Fig. 7.** An illustration of band diagram developed for a p-L-n junction before and after contact based on the band gaps of the materials at room temperature.
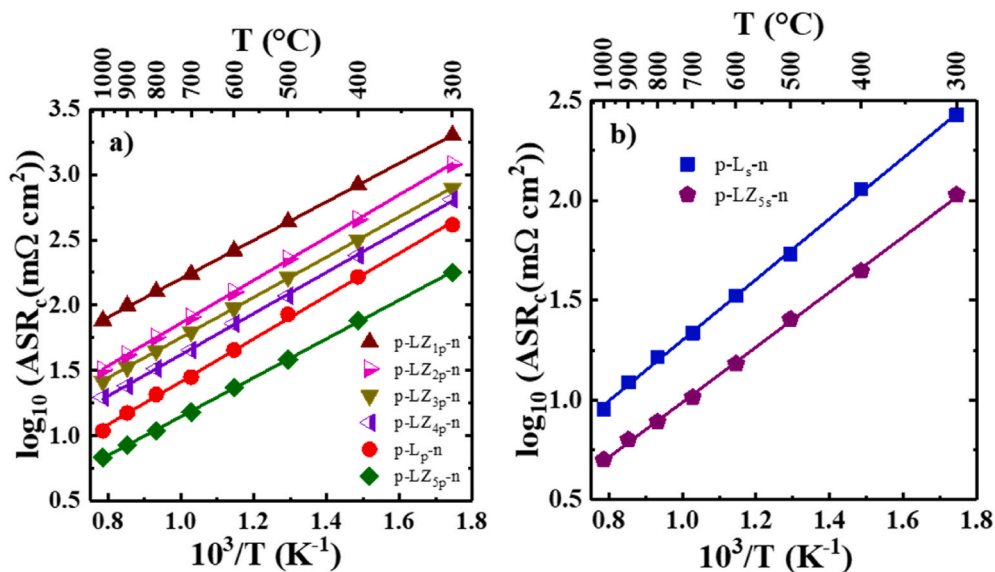
**Fig. 8.** Arrhenius plot for (a) five different LSC/Al–ZnO composite composition and pure LSC pellet interfaces and (b) junction with the printed interconnects of LSC and LZ$_5$.

**Table 1**

Volume composition of composite LSC/Al–ZnO and LSC interconnects and corresponding activation energy $E_a$ and preexponential factor $A_R$ calculated from Fig. 8(a).

| Sample | Vol% of LSC:Al–ZnO | $E_a$ (eV) | $A_R$ (mΩ cm$^2$) |
|---|---|---|---|
| LZ$_{1p}$ | 20:80 | 0.59 | 5.3 |
| LZ$_{2p}$ | 35:65 | 0.65 | 1.7 |
| LZ$_{3p}$ | 50:50 | 0.62 | 1.6 |
| LZ$_{4p}$ | 65:35 | 0.64 | 1.1 |
| LZ$_{5p}$ | 80:20 | 0.58 | 0.45 |
| LZ$_{5s}$ | 80:20 | 0.55 | 0.41 |
| L$_p$ | 100:00 | 0.63 | 0.60 |
| L$_s$ | 100:00 | 0.62 | 0.59 |

## Declaration of competing interest

The authors declare that they have no known competing financial interests or personal relationships that could have appeared to influence the work reported in this paper.

## Acknowledgements

## References

[1] J.G. Noudem, et al., Thermoelectric ceramics for generators, J. Eur. Ceram. Soc. 28 (1) (2008) 41–48.
[2] M. Zebarjadi, et al., Perspectives on thermoelectrics: from fundamentals to device applications, Energy Environ. Sci. 5 (1) (2012) 5147–5162.
[3] K. Xiong, et al., Electronic structures and stability of Ni/Bi2Te3and Co/Bi2Te3interfaces, J. Phys. Appl. Phys. 43 (11) (2010) 115303.
[4] D.K. Aswal, R. Basu, A. Singh, Key issues in development of thermoelectric power generators: high figure-of-merit materials and their highly conducting interfaces with metallic interconnects, Energy Convers. Manag. 114 (2016) 50–67.
[5] G.J. Snyder, et al., Thermoelectric microdevice fabricated by a MEMS-like electrochemical process, Nat. Mater. 2 (8) (2003) 528–531.
[6] S.-M. Choi, et al., Oxide-based thermoelectric power generation module using p-type Ca3Co4O9 and n-type (ZnO)7In2O3 legs, Energy Convers. Manag. 52 (1) (2011) 335–339.
[7] G. Skomedal, et al., Design, assembly and characterization of silicide-based thermoelectric modules, Energy Convers. Manag. 110 (2016) 13–21.
[8] R. He, G. Schierning, K. Nielsch, Thermoelectric devices: a review of devices, architectures, and contact optimization, Adv. Mater. Technol. 3 (4) (2018) 1700256.
[9] D. Muchilo, et al., Development of Mechanically and Chemically Stable Electrical Contacts for Thermoelectric Oxide Material, 2003, pp. 243–246.
[10] E. Reddy, et al., Fabrication and properties of four-leg oxide thermoelectric modules, J. Phys. Appl. Phys. 38 (2005) 3751.
[11] K. Arai, et al., Improvement of electrical contact between TE material and Ni electrode interfaces by application of a buffer layer, J. Electron. Mater. 41 (6) (2012) 1771–1777.
[12] W. Liu, et al., Current progress and future challenges in thermoelectric power generation: from materials to devices, Acta Mater. 87 (2015) 357–376.
[13] W. Liu, S. Bai, Thermoelectric interface materials: a perspective to the challenge of thermoelectric power generation module, J. Mater. 5 (3) (2019) 321–336.
[14] C.-H. Lim, et al., A study of electrodes for thermoelectric oxides, Electronic Mater. Lett. 9 (4) (2013) 445–449.
[15] R. Funahashi, et al., Ca2.7Bi0.3Co4O9/La0.9Bi0.1NiO3 thermoelectric devices with high output power density, Appl. Phys. Lett. 85 (6) (2004) 1036–1038.
[16] T.C. Holgate, et al., Characterization of the interface between an Fe–Cr alloy and the p-type thermoelectric oxide Ca3Co4O9, J. Alloys Compd. 582 (2014) 827–833.
[17] H. Kozuka, et al., Origin of high electrical conductivity in alkaline-earth doped LaCoO3, J. Mater. Chem. 22 (22) (2012) 11003–11005.
[18] T.D. Desissa, M. Schrade, T. Norby, Electrical properties of a p–n heterojunction of Li-doped NiO and Al-doped ZnO for thermoelectrics, J. Electron. Mater. 47 (9) (2018) 5296–5301.
[19] T.D. Desissa, et al., Inter-diffusion across a direct p-n heterojunction of Li-doped NiO and Al-doped ZnO, Solid State Ionics 320 (2018) 215–220.
[20] O.F. Kononchuk, Transient thermogravimetric measurement of chemical diffusion in La0.7Sr0.3CoO3−δ, ECS Proc. Vol. 1995–1 (1) (1995) 395–403.
[21] T. Ito, Q. Zhang, F. Saito, Synthesis of Perovskite-type lanthanum cobalt oxide nanoparticles by means of mechanochemical treatment, Powder Technol. 143–144 (2004) 170–173.
[22] G. Velciu, et al., LaCoO3 synthesis by intensive mechanical activation, Ceram. Int. 41 (2015) 6876–6881.
[23] T.V. Aksenova, L.Y. Gavrilova, V.A. Cherepanov, Phase equilibria at 1100°C in air and crystal structure of solid solutions in the system LaCoO3—SrCoO2.5—"SrNiO3"—"LaNiO3", Inorg. Mater. 40 (12) (2004) 1336–1340.
[24] F. Barbier, C. Monty, M. Déchamps, On the grain boundary diffusion of Co in NiO bicrystals, Philos. Mag. A 58 (3) (1988) 475–490.
[25] T.V. Thi, et al., High performance of Co-doped NiO nanoparticle anode material for rechargeable lithium ion batteries, J. Power Sources 292 (2015) 23–30.
[26] P. Hjalmarsson, M. Søgaard, M. Mogensen, Defect structure, electronic conductivity and expansion of properties of (La1−xSrx)sCo1−yNiyO3−δ, J. Solid State Chem. 183 (8) (2010) 1853–1862.
[27] J.-w. Seo, et al., A ZnO cross-bar array resistive random access memory stacked with heterostructure diodes for eliminating the sneak current effect, Appl. Phys. Lett. 98 (2011), pp. 233505–233505.
[28] I. Sta, et al., Fabrication and characterization of NiO/ZnO p-n junctions by sol-gel spin coating technique, in: 2012 First International Conference on Renewable Energies and Vehicular Technology, 2012, pp. 113–115.
[29] A. Kumar, D. Sivaprahsam, A.D. Thakur, Improvement of thermoelectric properties of lanthanum cobaltate by Sr and Mn co-substitution, J. Alloys Compd. 735 (2018) 1787–1791.

[30] K. Gaur, S.C. Verma, H.B. Lal, Defects and electrical conduction in mixed lanthanum transition metal oxides, J. Mater. Sci. 23 (5) (1988) 1725–1728.

[31] E. Iguchi, K. Ueda, H. Nakatsugawa, Electrical transport in La1-xSrxCoO3 (0.03≤x≤0.07) below 60 K, J. Phys. Condens. Matter 10 (40) (1998) 8999.

[32] D. Meziani, et al., Hydrogen evolution under visible light over LaCoO3 prepared by chemical route, Energy Convers. Manag. 82 (2014) 244–249.

[33] B.-T. Zhang, et al., Hot electron injection: an efficacious approach to charge LaCoO3 for improving the water splitting efficiency, Appl. Catal. B Environ. 219 (2017) 432–438.

[34] W. Haron, et al., A simple synthesis and characterization of LaMo3 (M=Al, Co, Fe, Gd) perovskites via chemical co-precipitation method, Songklanakarin J. Sci. Technol. 40 (2018) 484–491.